 doi:10.20944/preprints202208.0462.v1

Original Article

Small Extracellular Vesicles from Hypoxic Triple-Negative Breast Cancer Cells induce Oxygen-dependent Cell Invasion

Bianca Cruz Pachane[1]; Ana Carolina Caetano Nunes[1]; Thais Regiani Cataldi[2]; Kelli Cristina Micocci[3]; Bianca Caruso Moreira[1]; Carlos Alberto Labate[2]; Heloisa Sobreiro Selistre-de-Araujo[1] & Wanessa Fernanda Altei[4,5*]

[1] Biochemistry and Molecular Biology Laboratory, Department of Physiological Sciences, Universidade Federal de São Carlos – UFSCar, São Carlos, SP, Brazil.
[2] Max Feffer Plant Genetics Laboratory, Department of Genetics, University of São Paulo – ESALQ, Piracicaba, SP, Brazil
[3] Center for the Study of Social Insects, São Paulo State University "Julio de Mesquita Filho", Rio Claro, SP, Brazil
[4] Molecular Oncology Research Center, Barretos Cancer Hospital, Barretos, SP, Brazil
[5] Radiation Oncology Department, Barretos Cancer Hospital, Barretos, SP, Brazil
* Correspondence: wanessa.altei@hospitaldeamor.com.br

Abstract: Hypoxia, a condition of low oxygenation frequently found in triple-negative breast tumors (TNBC), promotes extracellular vesicle (EV) secretion and favors cell invasion, a complex process in which cell morphology is altered, dynamic focal adhesion spots are created, and ECM is remodeled. Here, we investigated the invasive properties triggered by TNBC-derived hypoxic small EV (SEVh) *in vitro* in cells cultured under hypoxic and normoxic conditions, using phenotypical and proteomic approaches. SEVh characterization demonstrated increased protein abundance and diversity over normoxic SEV (SEVn), with enrichment in pro-invasive pathways. In normoxic cells, SEVh promotes invasive behavior through pro-migratory morphology, invadopodia development, ECM degradation and matrix metalloprotease (MMP) secretion. Proteome profiling of normoxic cells exposed to SEVh determined enrichment in metabolic processes and cell cycle, modulating cell health to escape apoptotic pathways. In hypoxia, SEVh was responsible for proteolytic and catabolic pathway inducement, interfering with integrin availability and gelatinase expression. Overall, our results demonstrate the importance of hypoxic signaling via SEV in tumors for the early establishment of metastasis.

Keywords: Hypoxia; Extracellular vesicles; Breast Cancer; Cell Invasion

1. Introduction

In most solid tumors, the establishment of hypoxia (low oxygen tissue perfusion) is a consequence of increased tumor mass due to cell proliferation during cancer progression [1]. Both primary and metastatic breast adenocarcinomas have hypoxia as a feature aiding tumor survival and drug resistance, thus impairing overall patient survival and successful therapeutics [2]. The stress caused by the lack of oxygen, either acute, intermittent or continuous, regulates metabolic and cellular responses via the activation of the hypoxia-inducible factor (HIF) pathway which directly interferes with survival, angiogenesis, invasiveness, stemness and resistance to chemotherapy [3–6].

The exposure of breast tumor cells to hypoxia promotes the secretion and biogenesis of extracellular vesicles (EV), while also favoring HIF-1α signaling [1,7,8]. In triple-negative breast cancer (TNBC), a highly aggressive breast cancer subtype which lacks receptors for estrogen (ER-), progesterone (PR-) and HER2 [7,9], EVs have been highlighted in aiding pro-tumoral responses such as pre-metastatic niche establishment [1], directed migration and organotrophic metastasis [10], and transmitting signals for potentiating malignant proprieties on the tumor microenvironment [11]. EVs separated from cells undergoing oxygen stress were previously described to increase pro-angiogenic

 doi:10.20944/preprints202208.0462.v1

signaling and survival in endothelial cells [12,13], and to promote epithelial-to-mesenchymal transition (EMT) and metastasis, especially aiding cell migration and invasion [8,13].

Active and directed migration of tumor cells through adjacent tissues, resulting from a combination of processes including extracellular matrix (ECM) remodeling, dynamic focal adhesion spots and F-actin cytoskeleton polarization, defines the behavior of cell invasion. This is considered an early step of metastasis that may favor intravasation, extravasation and the colonization of a new metastatic niche [14,15]. As many complex biological processes, invasion relies heavily on cytoskeleton arrangement, involving tubulin-rich structures called invadopodia [16], and communication between the intracellular and extracellular compartments, which may be performed by transmembrane adhesion molecules such as integrins [14]. Interestingly, invadopodia formation enhances exosome secretion, indicating a key role of these nanoscale structures in cell invasion [17].

To investigate the invasive properties of TNBC-derived, hypoxic small extracellular vesicles (SEVh) in tumor cells *in vitro*, we compared the responses obtained on cell line MDA-MB-231 in normoxia and hypoxia and addressed: (1) phenotypic alterations elicited by SEVh; (2) ECM remodeling by gelatinases (matrix metalloproteases MMP2 and MMP9); (3) direct interference of SEVh in *in vitro* invasion and (4) proteomic profiling of cells after SEVh exposure.

2. Materials and Methods

Cell Lines and Culture Conditions

Triple-negative breast cancer cells (MDA-MB-231) were purchased from ATCC and maintained in DMEM supplemented with glucose (4.6 g/l), sodium pyruvate (10 mg/l) and fetal bovine serum (10% FBS) at 37 °C, 5% CO_2. A hypoxic atmosphere (1% O_2, 5% CO_2, 37 °C) was set in a H35 Hypoxystation (Don Whitley Scientific) and cells were incubated immediately after plating and for no longer than 4 days. EV-depleted FBS (UC-FBS) was collected after ultracentrifugation (18 h, 100,000 *g*, 4 °C - Type 45Ti rotor, Optima XE-90 ultracentrifuge, Beckman Coulter), and filtration through a 0.22µm syringe filter.

EV isolation by differential ultracentrifugation

MDA-MB-231 ($1.6x10^4$ cells/cm^2) were plated in DMEM 10% UC-FBS and incubated in hypoxia for 24 h. Culture media was exchanged to Opti-MEM reduced serum media (Gibco) for a further 48-hour incubation. Conditioned media was collected and submitted to a 4-step differential centrifugation process, in order to sediment live cells (300 *g*, 10 min, 4 °C; F-35-6-30 rotor, Eppendorf 5430R), large-EV (LEV - 2,000 *g*, 30 min, 4 °C; F-35-6-30 rotor, Eppendorf 5430R), medium-EV (MEV - 10,000 *g*, 30 min, 4 °C; Type 45Ti rotor, Beckman Coulter Optima XE-90) and small-EV (150,000 *g*, 2 h, 4 °C; Type 45Ti rotor, Beckman Coulter Optima XE-90). EV pellets were collected, washed and resuspended in filtered PBS. This procedure was replicated under normal culture conditions (~20% O_2, 5% CO_2, 37 °C) for comparison.

Nanoparticle Tracking Analysis

EV size and abundance were assessed on Nanosight NS300 (Malvern Panalytical, Malvern, UK) with a NTA software (version 2.3, build 0033). EV samples were diluted in ultrapure water (1:1,000 to 1:4,000) and analyzed by five 60-second captures, with parameters: screen gain: 2.0, camera level: 14, blur: auto, max jump distance: 14.6, min track length: auto. For processing, we used screen gain 10.0 and detection threshold 4.0.

Transmission electron microscopy (TEM)

EVs were diluted (1:2) in PBS and deposited in copper grids covered with formvar and carbon (Lot 051115, 01800 F/C, 200 mesh Cu, Ted Pella Inc.) for 20 min, RT. Samples were fixed in 2% paraformaldehyde (PFA) in 0.2 M PBS, pH 7.4 for 20 min, RT, followed by extensive washes in deionized water. Grids were exposed to 4% Uranyl-acetate (pH 4)

Preprints (www.preprints.org) | NOT PEER-REVIEWED | Posted: 26 August 2022 doi:10.20944/preprints202208.0462.v1

and 2% methylcellulose solution for 10 min on ice and in the dark [18]. After dry, samples were visualized in a FEI TECNAI G² F20 HRTEM microscope on 40,000x magnification.

Protein quantification

Isolated EV samples, cell lysates and conditioned media were quantified using either a microBCA kit (Thermo Fischer Scientific) or a standard BCA assay kit (Thermo Fisher Scientific), according to manufacturer's instructions. Assays were considered successful if BSA standard curve reached $R^2 < 0.99$.

Experimental design

Cells (MDA-MB-231, 10^6 cells/well) were plated in triplicates on a 6-well plate, using DMEM 10% UC-FBS, and incubated for 24 h in hypoxia or normoxia. Cell media was replaced to contain SEVh (5 μg/ml) for further 24 h incubation, followed by collection. Untreated controls (i.e., PBS) were kept in parallel.

Cell lysate

Cells were collected by scraping in ice-cold PBS, pelleted (7,800 rpm, 12 minutes, 4 °C) and resuspended in lysis buffer (50 mM Tris-HCl, pH 7.4; 1% tween-20, 0,25% deoxycholate, 150 mM NaCl, 1 mM EDTA, 1 mM sodium orthovanadate, 1 mM sodium fluoride, 0.1 mM PMSF, 1 μg/ml aproptinin and 1 μg/ml leupeptinin) for 2h on ice. Samples were centrifuged (14,000 rpm, 20 min, 4°C) to collect the supernatant.

Western Blotting

Samples (10 μg) were mixed with Laemmli sample buffer, boiled (5 min, 100 °C) and applied to SDS-PAGE gels with Precision Plus Dual Color (Bio-Rad) as loading control. Protein samples were separated by electrophoresis, transferred to nitrocellulose membranes (0.45 μm, Bio-Rad) and stained with Ponceau S dye for 2 minutes for quality control. Non-specific bindings were blocked with 3% BSA in Tween-TBS buffer (140 mM NaCl, 2.6 mM KCl, 25 mM Tris pH 7.4, 0.05% Tween 20) for 1 hour prior to probing with primary antibodies for: Alix (1:1000, 186429 Abcam), Calnexin (1:1000, mAb 2679 Cell Signaling), CD63 (1:1000, 59479 Abcam), Flotillin-1 (1:1000, 61020 BD Biosciences), HIF-1α (1:1000, 51608 Abcam), integrin β1 (1:2000, 179471 Abcam), integrin β3 (1:1000, 119992 Abcam; 1:1000, 34409 Abcam), MMP-2 (1:1000, 92536 Abcam), MMP-9 (1:500, 38898 Abcam). Appropriate secondary antibodies were applied for 1h: IgG Goat anti-Mouse HRP (1:10,000, 97040 Abcam) and IgG Goat anti-Rabbit HRP (1:10,000, 97051 Abcam; 1:15,000, 205718 Abcam). Membranes were revealed with ECL substrate (1705061 Bio-Rad; 34096 Thermo Fisher Scientific) for 3 minutes, scanned on a ChemiDoc imaging system (Bio-Rad) and analyzed using FIJI[19]. For constitutive protein probing, membranes were either cut or stripped with glycine, 0.1% SDS and 1.0% Tween 20 buffer (pH 2.2), washed, blocked, and exposed to anti-GAPDH (1:10,000, 181602 Abcam).

Protein Extraction

Approximately 200 μg of protein were applied to Amicon®Ultra 0.5 column (3000 NMWL, Millipore), centrifuged (14,000 *g*, 30 min, 4°C), concentrated (1,000 *g*, 2 min, 4°C) and re-quantified (BCA). Proteins were solubilized with RapiGest SF (0.2%, Waters) at 80°C for 15 min, followed by addition of dithiothreitol (100 mM, Bio-Rad) for 30 min, 60°C and iodoacetamine (300 nM, GE) for 30 min, RT. After overnight digestion in trypsin solution in 50 mM NH_4HCO_3 (0.05 μg/μl) at 37 °C, samples were transferred to MS vials and lyophilized.

Label-free LC-MS/MS proteomics

LC–MS was performed on a NanoElute system (Bruker Daltonik) coupled online to a hybrid TIMS-quadrupole TOF mass spectrometer[20] (Bruker Daltonik timsTOF Pro) via a nano-electrospray ion source (Bruker Daltonik Captive Spray). For long gradients runs (2 hours total run), approximately 200 ng of peptides were separated on an Aurora column 25 cm × 75 μm ID, 1.9 um reversed-phase column (Ion Opticks) at a flow rate of 300 nL min^{-1} in an oven compartment heated to 50 °C. To analyze samples from whole-proteome digests, we used a gradient starting with a linear increase from 2% B to 17% B over 60 min,

 doi:10.20944/preprints202208.0462.v1

followed by further linear increases to 25% B in 30 min and to 37% B in 10min. Finally, to 95% B in 10 min which was held constant for 10 min. Column was equilibrated using 4 volumes of solvent A. The mass spectrometer was operated in data-dependent PASEF [21] mode with 1 survey TIMS-MS and 10 PASEF MS/MS scans per acquisition cycle. We analyzed an ion mobility range from $1/K_0$ = 1.6 to 0.6 Vs cm^{-2} using equal ion accumulation and ramp time in the dual TIMS analyzer of 100 ms each. Suitable precursor ions for MS/MS analysis were isolated in a window of 2 Th for m/z < 700 and 3 Th for m/z > 700 by rapidly switching the quadrupole position in sync with the elution of precursors from the TIMS device. The collision energy was lowered stepwise as a function of increasing ion mobility, starting from 20 eV for $1/K_0$ = 0.6 Vs cm^{-2} and 59 eV for $1/K_0$ = 1.6 Vs cm^{-2}. We made use of the m/z and ion mobility information to exclude singly charged precursor ions with a polygon filter mask and further used "dynamic exclusion" to avoid re-sequencing of precursors that reached a "target value" of 20,000 a.u. Ion mobility dimension was calibrated linearly using three ions from the Agilent ESI LC/MS tuning mix (m/z, $1/K_0$: 622.0289, 0.9848 Vs cm^{-2}; 922.0097, 1.1895 Vs cm^{-2}; and 1221.9906, 1.3820 Vs cm^{-2}).

Bioinformatic analysis and data enrichment

MS scans were cross-referenced with UniProt Annotated Complete Human Proteome [22] using MaxQuant [23]. Data processing in Perseus [24] removed reverse proteins, possible contaminants and single-sample proteins. Spectra values were normalized by total ion count (TIF = 10^6 × intensity/∑ total intensity), transformed by -log10, and scaled following Paretto's parameter. Principal component analysis (PCA), hierarchical clustering and univariate statistical analysis were performed in MetaboAnalyst (v. 5.0) [25]. Data enrichment and functional analysis were executed on databases STRING [26] and Reactome [27] (minimum requirements: medium confidence interaction score=0.4; p<0.05). False discovery rates (FDR) were considered as confidence requirements on enrichment analysis. Mass spectrometry proteomics data have been deposited to the ProteomeXchange Consortium (http://proteomecentral.proteomexchange.org) via the PRIDE partner repository [28] with the dataset identifier PXD035244.

Gelatin Zymography

Samples (10 μg) were prepared with 50% non-reducing sample buffer and loaded into 10% gelatin (100 μg/ml) SDS-PAGE gels for electrophoresis at 4°C. Gels were washed with 2.5% Triton X-100 for 40 minutes, RT and submersed in refolding buffer (20 mM Tris, 5 mM $CaCl_2$, 1 μM $ZnCl_2$, pH 8.0) for 20h, 37°C. Gels were dyed using Coomassie Brilliant Blue overnight and de-stained for band revelation [29]. Gels were documented (ChemiDoc, Bio-Rad) and clear bands were quantified on FIJI [19]. For quality control, a loading sample was used in all gels to reduce differences in dye efficiency. Each sample was run twice in different gels (n=3).

Integrin Immunophenotyping by Flow Cytometry

Cells were scraped in ice-cold PBS, pelleted by centrifugation (8 min at 1,200 rpm, 4 °C) and resuspended in PBS for binding with primary antibodies: anti-integrin β1 (1 μg/sample, 13590 Santa Cruz Biotechnology) and anti-integrin β3, (0.125 μg/sample, 110131 Abcam). After 1h incubation at 4 °C, tubes were washed twice with PBS (1,200 rpm, 10 min, 4°C) before secondary antibody probing (45 min, 4 °C - Goat Anti-Mouse IgG H&L [FITC], 1:1,000, 6785 Abcam). Samples were washed twice with PBS (1,200 rpm, 10 min, 4 °C) and resuspended for flow cytometry analysis on BD Accuri™ C6 (BD Biosciences). A total of 15,000 events were captured in each replicate (n=3). Doublets were removed using standard gating technique (Figure S1a) and singlets were displayed in histograms for median determination. Population comparison was performed on FlowJo (v.10.8.1) using the super enhanced Dmax subtraction (SE Dymax) as comparative parameter.

Matrigel invasion assay

Preprints (www.preprints.org) | NOT PEER-REVIEWED | Posted: 26 August 2022 doi:10.20944/preprints202208.0462.v1

An invasion chamber was assembled using 8.0 μm-pore inserts (662638 Greiner) coated with Matrigel (Corning) for 2h at 37 °C, installed in a 24-well plate (662160-01 Greiner). Cells (10^5/well) were treated with SEVh (5 μg/ml) in FBS-free media on ice and applied to the top chamber. Inserts were assembled atop wells containing DMEM 10% FBS (negative control: FBS-free DMEM) and incubated for 6 and 16h in normoxia or hypoxia (1% O_2). Membranes were fixed with 4% PFA for 10 min, washed and cleaned with a cotton swab. Cell nuclei was stained with DAPI (0.7 ng/μl) for 10 min. Membranes were detached and assembled in slides for epifluorescence imaging (ImageXpress Micro, Molecular Devices) at 10x magnification, followed by automated nuclei count. Cell invasion index was calculated as the ratio between total nuclei count from groups and the total nuclei count from untreated, normoxic cells.

Fluorescent gelatin degradation assay

Round coverslips were coated with poly-L-lysine (0.1 mg/ml) for 20 min, RT, cross-linked with 0.5% glutaraldehyde for 15 min and covered with a thin layer of fluorescent gelatin (G13187 Molecular Probes, 0.2 mg/ml) overnight at 4 °C. MDA-MB-231 (50,000 cells/well) were treated with SEVh (5 μg/ml) and plated in FBS-free DMEM (positive control: DMEM 10% FBS). Cells were incubated for 24 and 48 h in normoxia or hypoxia, protected from light. Cells were fixed with 4% PFA for 10 min, permeabilized for 5 min with 0.1% Triton X-100 and blocked for 1 h with 1% BSA-PBS, RT. Tubulin was immunoprobed (5 μg/ml; 80779 Abcam) overnight at 4°C, followed by a 1-hour incubation with secondary antibody AlexaFluor 647 (1 μg/ml; 150115 Abcam). DAPI (0.7 ng/μl) was used for nuclei staining. Slides were assembled using Prolong™ mounting media (Thermo Fisher Scientific). Epifluorescence images were acquired for field analysis (ImageXpress Micro, Molecular Devices) under 20x magnification, and representative imaging was performed under 60x magnification in a confocal microscope (Olympus FV10i). We quantified the total degraded area over a 72x72 μm frame, then normalized the values by cell count.

Cell morphology assay

Cells were plated on round uncoated plates or coverslips coated with gelatin (0.2 mg/ml) or Matrigel (1:1, v/v). After incubation in normoxia or hypoxia for 24h or 48h, samples were fixated with 4% PFA for 10 min, RT, washed and permeabilized with 0.1% Triton X-100 for 5 min, RT. Cell nuclei and F-actin were stained with DAPI (0.7 ng/μl) + 2,5% Phalloidin-FITC for 20 min. Image acquisition was performed at 20x magnification (IN Cell Analyzer 2200, GE Healthcare). Parameters of cell circularity, aspect ratio (AR) and perimeter/area ratio (Figure S1B) were calculated on FIJI [19] (n=300).

Apoptosis assay

Cells were centrifuged (400 *g*, 5 min, 4°C), washed on iced PBS (2,000 *g*, 5 min, 4 °C) and scrapped in binding buffer for staining with Annexin V-PE and 7AAD (7-aminoactinomycin), using the BD Pharmingen™ PE Annexin V Apoptosis Detection Kit I (Cat 559763, Lot 8086787, BD Biosciences). Cells were centrifuged (2,000 rpm, 5 min, 4°C) and resuspended in binding buffer for flow cytometry analysis on BD Accuri™ C6 (BD Biosciences), where 15,000 events were analyzed. Experimental controls included unstained and untreated cells in both incubation settings, single-stained and double-stained controls (Figure S1c). Assay was conducted with technical duplicates and biological triplicates.

Total RNA extraction and cDNA synthesis

Cells were scrapped in ice-cold TRIzol (Invitrogen) and mixed with chloroform at RT for 15 min. After centrifugation (12,000 x *g*, 10 min, 4 °C), the upper translucent fraction was collected and mixed to isopropanol for 10 min, RT. Samples were centrifuged at 12,000 rpm for 10 min, 4 °C and washed twice with 75% ethanol (7,500 rpm, 5 min, 4 °C). After dried, pellets were resuspended in ultrapure water and quantified (NanoDrop 2000, Thermo-Fisher Scientific). RNA samples were treated with DNase I (#18068-015, Invitrogen) and reverse transcription was performed using the *High-capacity cDNA Reverse Transcription* kit (Applied Biosystems).

 doi:10.20944/preprints202208.0462.v1

Gene expression by RT-qPCR

Primers for the analysis of HIF-1α (NM_001243084.2), MMP-2 (NM_004530.4), MMP-9 (NM_004994.2), integrin β1 (NM_133376.3) and integrin β3 (NM_000212.3) expression by qPCR were designed using the online tool (http://www.ncbi.nlm.nih.gov/tools/primer-blast). DNA sequences were checked using Blast (http://blast.ncbi.nlm.nih.gov/Blast.cgi). Primer sequences for targeted genes were: HIF1A (F: AAAATCTCATCCAAGAAGCC; R:AATGTTCCAATTCCTACTGC), ITGB1 (F: ATTCCCTTTCCTCAGAAGTC; R: TTTTCTTCCATTTTCCCCTG), ITGB3 (F: CTCCGGCCAGATGATTC; R: TCCTTCATGGAGTAAGACAG), MMP2 (F: AGGACCGGTTCATTTGGCGG; R: TGGCTTGGGGTACCCTCGCT) and MMP9 (F: CGCTACCACCTCGAACTTTG; R: GCCATTCACGTCGTCCTTAT). Housekeeping genes GAPDH (F: ACAGTTGCCATGTAGACC; R: TTGAGCACAGGGTACTTTA) and HPRT (F: TGACACTGGCAAAACAATGCA; R: GGTCCTTTTCACCAGCAAGCT) were used as normalizers. Reactions were set to start at 95 °C for 10 min, followed by 40 cycles of 95 °C, 15 s; 59-68 °C for 30s; and 72 °C for 30 s. Melt curve was produced by increasing temperature from 65°C to 95 °C in 0.5°C increments every 30s. PCR products were determined based on Ct values (threshold cycle), in which each gene expression variation is equal to $2^{-\Delta\Delta Ct}$ [30].

Statistical analysis

All assays were performed in technical triplicates and at least three independent experiments. Data was submitted to ROUT's outlier detection test and normality tests (Shapiro-Wilk for n<9, D'Agostino-Pearson omnibus K2 for n≥9). In case of lognormality, datasets were transformed in $\log_{10}$. Parametric data was analyzed using ANOVA one-way with Tukey's multiple comparison *post-hoc*. Non-parametric data were tested using Kruskal-Wallis analysis of variance, with Dunn's multiple comparison post-test. Values of $p<0.05$ were considered statistically relevant. Results are presented as mean ± standard deviation (SD) or standard error of mean (SEM) if parametric, and median ± interquartile range if non-parametric. Data analysis and graph design were made on GraphPad Prism (v. 9.3).

3. Results

SEVh isolation and characterization

Each EV isolation process was performed and characterized following MISEV2018 guidelines [31], and all relevant data was submitted to the EV-TRACK knowledgebase (EV-TRACK ID: EV220177) [32]. On average, EVs were isolated from $1.94x10^7 \pm 0.48x10^6$ cells in hypoxia, with 94% ± 4.3% viable cells. Under normoxic culture conditions, EVs were separated from $1.98x10^7 \pm 0.54x10^6$ cells with 96.3% ± 2.6% cell viability.

Higher concentrations of protein were detected on hypoxic EV when compared to their normoxic counterparts (Figure 1a). After normalizing the protein concentration by the final volume of each sample, we obtained a total protein content of 270.5 ± 93.9 μg in hypoxic SEV (SEVh), and 109.0 ± 41.47 μg in normoxic SEV (SEVn). For MEV, protein levels varied from 28.8 ± 11.9 μg in normoxia to 76.8 ± 42.2 μg in hypoxia.

Label-free LC-MS proteomic analysis identified 10 EV biomarkers [31] (ADAM10, ALIX, CD47, CD63, CD81, CD82, CD9, FLOT-1, FLOT-2 and TSG101) in all SEV samples, with undistinguished profile between SEVh and SEVn (Figure 1b). We validated some markers by western blotting, in which an enrichment of proteins Alix, CD63 and flotillin-1 in SEV samples from hypoxic and normoxic conditions was observed as expected (Figure 1c). Flotillin-1 was also identified in all LEV from both groups and MEV from hypoxia. Calnexin, serving as negative control, was only identified on cell lysate and LEV samples, albeit faintly. None of the proteins were found on the leftover condition media for either group. Hence, our object of study, SEVh, has a simplified protein profile of Alix+/CD63+/FLOT-1+/CANX-.

Preprints (www.preprints.org) | NOT PEER-REVIEWED | Posted: 26 August 2022 doi:10.20944/preprints202208.0462.v1

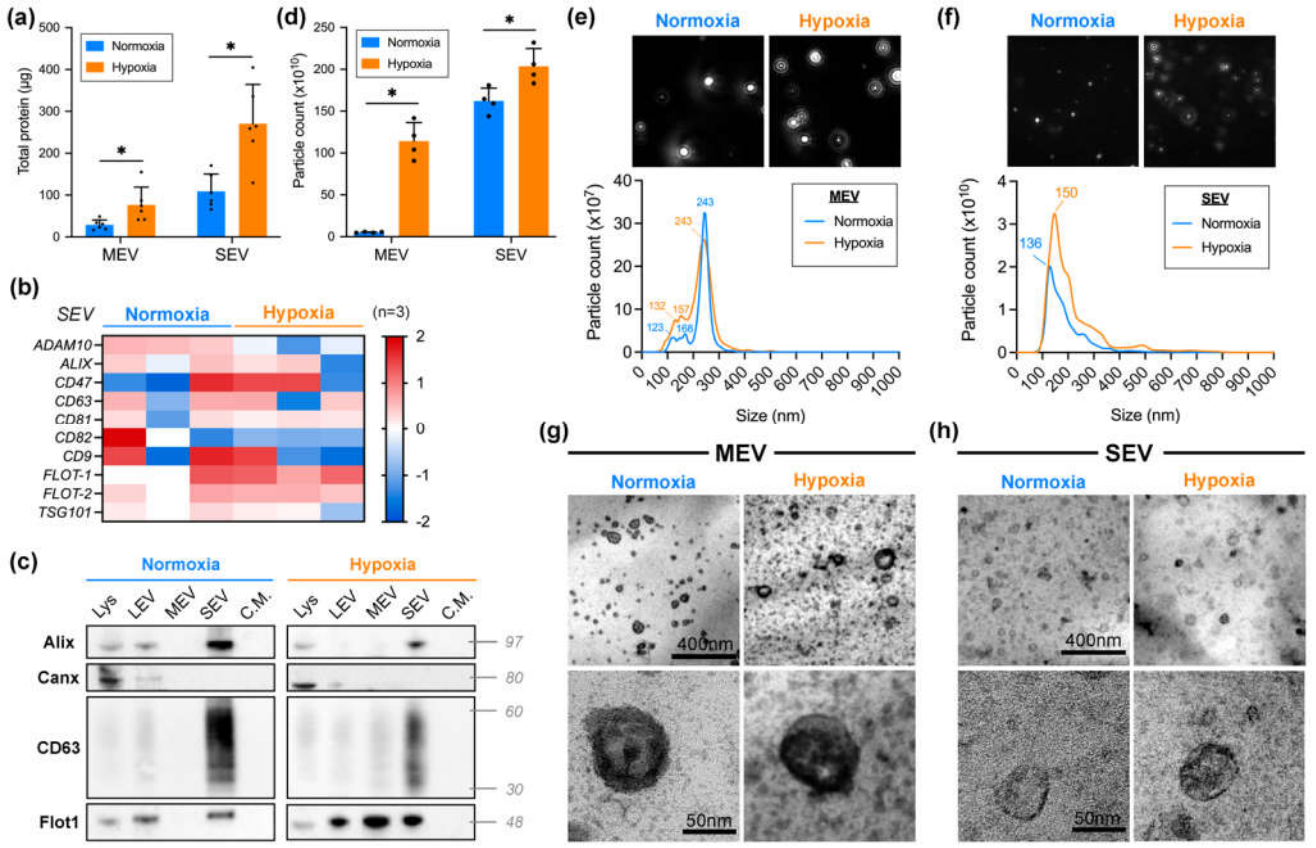

Figure 1. Isolation and characterization of EVs. (a) Total protein content for normoxic (blue) and hypoxic (orange) MEV and SEV. Data presented as mean ± SD (standard deviation). (b) SEV biomarker profile obtained via proteomic analysis. Each column indicates a biological replicate (n=3). (c) Immunoblotting membranes probed for proteins Alix, calnexin (Canx), CD63 and flotillin-1 (Flot1) containing samples of cell lysate (Lys), LEV, MEV, SEV, and the leftover conditioned media (C.M.) of EV isolations. (d) Particle count for MEV and SEV (mean ± SD). (e-f) Mean vesicle size dispersion for (e) MEV and (f) SEV (n=5). (g-h) Transmission electron microscopy images of broad field and individual (g) MEV and (h) SEV. Scale bar: 400 nm (top), 50 nm (bottom) *p<0.05

Particle analysis confirmed the overall abundance of hypoxic EVs when compared to their normoxic peers (Figure 1d). After normalizing particle count by final sample volume, hypoxia increased total particle count of SEV by 25% (SEVh = $2.03x10^{12}$ ± $2.1x10^{11}$ particles; SEVn = $1.62x10^{12}$ ± $1.5x10^{11}$ particles). A wider difference was observed in MEV samples ($5.23x10^{10}$ ± $5.8x10^{9}$ particles in normoxia, $1.14x10^{12}$ ± $2.2x10^{11}$ particles in hypoxia). NTA analysis provided a histogram displaying MEV (Figure 1e) and SEV (Figure 1f) size dispersion by particle count, which established their nomenclature: the mode for hypoxic and normoxic MEV was 243 nm whereas for SEV samples, it ranged from 136-150 nm.

Transmission electron microscopy allowed for visualization of broad range and individual MEV (Figure 1g) or SEV (Figure 1h). EVs presented typical morphology, adequate abundance, and sizes according to their nomenclature.

SEVh proteome is enriched with components of pro-invasive signaling pathways

Comparative label-free proteome of SEV samples identified a total of 2390 proteins, of which 2347 were found in hypoxia and 1278 in normoxia. A total of 1112 unique proteins were enriched in SEVh, contrasting to 43 in SEVn, and 1235 proteins were shared among both groups (Figure 2a). Principal component analysis (PCA) differentiated SEVh and SEVn, clustering replicates according to each group (Figure 2b) with principal

Preprints (www.preprints.org) | NOT PEER-REVIEWED | Posted: 26 August 2022 doi:10.20944/preprints202208.0462.v1

component (PC) values corresponding to 58.7%, 22.1%, 10.1%, 5.7% and 3.3% of designated variance.

Univariate analysis identified 552 statistically relevant proteins between SEVh and SEVn (p<0.05). The top 144 proteins (p<0.01) were considered for enrichment analysis (Figure 2c; Table S1). The most significantly upregulated protein of SEVh is ISG15 (FDR: $9.59x10^{-6}$), a ubiquitin-like protein previously linked to integrin-mediated cell invasion [33]. Other distinguished species found were mTOR ($3.6x10^{-4}$) and its regulator, RPTOR ($1.05x10^{-3}$), critical for controlling cancer metabolism [34]; and structural proteins like microtubule-associated proteins 1B, 4 and RB ($1.15x10^{-3}$; $1.78x10^{-3}$; $7.3x10^{-3}$, respectively). Two protein families were abundant in SEVh: the SMADs ($1.12x10^{-3}$), related to the activation of TGF-β pathway [35], and RGDPs ($1.67x10^{-3}$), predicted to act on the nuclear pore and to aid GTPase activity [36].

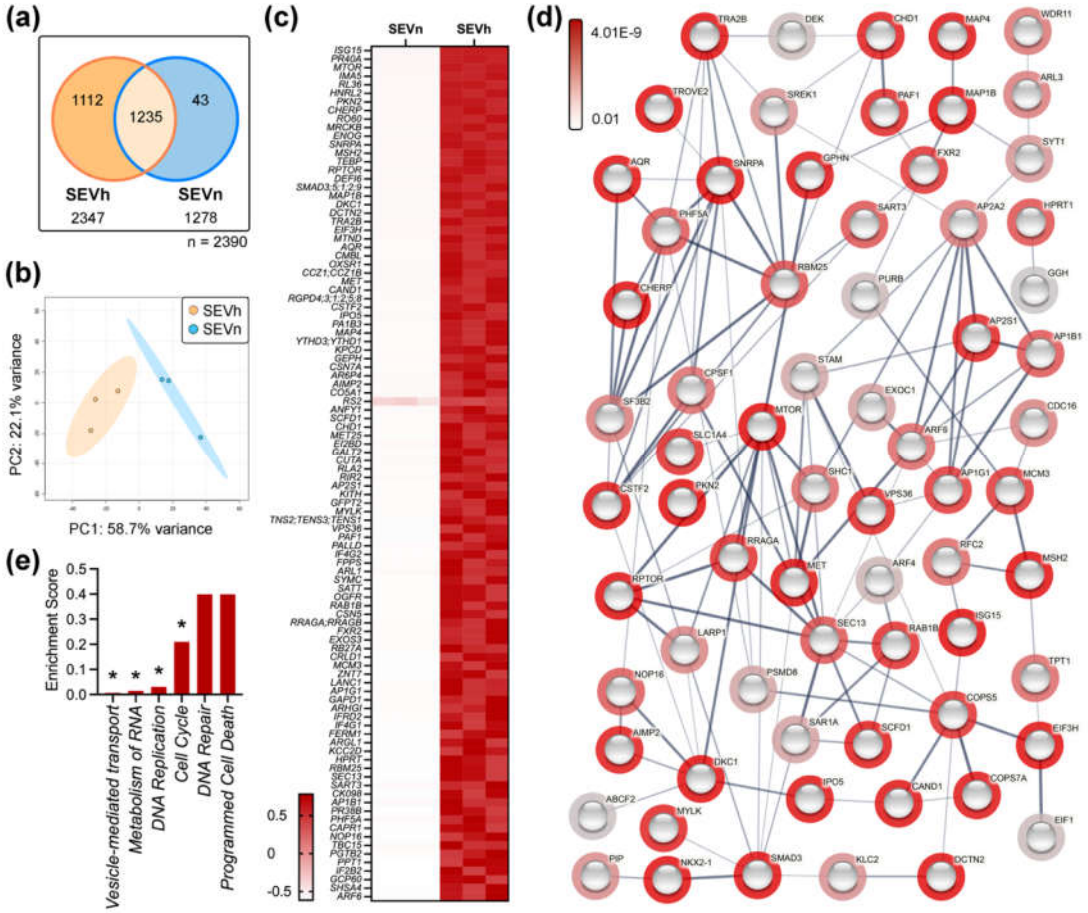

Figure 2. Comparative SEV proteomic profiling (a) Venn's diagram of protein distribution in SEVs (b) Principal component analysis (PCA) score plot (c) Heatmap of top 100 proteins differentially expressed in SEVh (p<0.01) (d) Interaction map of top 144 differentially expressed proteins in SEV samples with hidden disconnected nodes, created on String-DB. Halos indicate the strength of p values from the statistical analysis of normalized data (red to gray). Strings shown as confidence network edges, with soft lines for medium confidence (0.4), regular lines for high confidence (0.7) and bold lines for highest confidence (0.9) (d) Enrichment analysis on Reactome indicate upregulation of pathways from vesicle-mediated transport, metabolism of RNA, DNA replication and cell cycle in SEVh, compared to SEVn. *p<0.05

Both mTOR and TGF-β signaling pathways, alongside pro-angiogenic VEGFA/VEGFR2, were significantly favored in SEVh samples. Our analysis found an enrichment of four proteins of the mTOR pathway (RRAGB, RPTOR, MTOR and RRAGA;

 doi:10.20944/preprints202208.0462.v1

FDR: 2.7x10^{-3}), five of the TGF-β pathway (SMAD2, SMAD3, SMAD9, SMAD1 and SMAD5; FDR: 3.5x10^{-3}), and eleven of the VEGFA/VEGFR2 pathway (ABCF2, FXR2, AP2S1, SHC2, ARF6, ARF4, MTOR, CDC42BPB, STAM, SHC1 and EIF3H; FDR: 3.7x10^{-3}). We identified that pathways related to vesicle-mediated transport (6.7E-03), RNA metabolism (1.5x10^{-2}), DNA replication (3.01x10^{-2}) and cell cycle (0.21) were statistically upregulated in SEVh (Figure 2e).

SEV-h signaling triggers long-term MDA-MB-231 invasion

SEVh interference with TNBC invasion was assessed *in vitro* using two methods: i) a transwell invasion assay with matrigel coating (Figure 3a), and ii) a fluorescent gelatin-covered coverslip, in which invasion was assessed by matrix degradation (Figure 3b). Matrigel invasion was induced by hypoxia alone and by SEVh treatment in normoxia after 16h, with non-statistical tendencies observed as early as 6h (Figures 3a, S2a). Interestingly, invasion was not induced in hypoxic cells exposed to SEVh, indicating that oxygen may be necessary to promote SEVh-mediated invasion. Similar results were observed on gelatin invasion, where matrix degradation was not promoted by SEVh treatment in hypoxia (Figure 3b), thus highlighting the importance of oxygen for SEVh-mediated invasiveness.

SEVh signaling in normoxia was a driving force for gelatin invasion after 48h, as was hypoxia (FBS- group), with non-statistical tendencies appearing after 24h (Figures 3b, S2b). The size and abundance of degradation spots on the fluorescent matrix varied between groups (Figure 3c) and was more pronounced in normoxic SEVh-treated cells (Figure 3d). We expected spots to be presented on cell periphery, yet despite the abundance of degradation in this group, few cells colocalized with them, which suggests that cellular motility was favored in this setting.

Since gelatinase activity was detected, we investigated the effects of SEVh and/or hypoxia in MMP-2 and MMP-9. Our results suggest a significant increase in activity of soluble MMP-2 (Figure 3e) and MMP-9 (Figure 3f) 48h after SEVh exposure in normoxia. Intriguingly, MMP-2 was detected as a 52 kDa band on SEVh-treated groups, whereas a regular 62 kDa band was found on positive controls (FBS+). No gelatinase activity was detected after 24h (Figures S2d,e). Regarding gene expression, SEVh signaling and/or hypoxia drastically increased MMP-2 (Figure 3g), whereas MMP-9 was diminished only after SEVh exposure in hypoxia (Figure 3h). Gene expression results were not corroborated by protein expression – both MMP-2 (Figure 3i) and MMP-9 (Figure 3j) were boosted only in hypoxic SEVh-treated cells. These results suggest SEVh and hypoxia signaling are interfering in separate regulatory mechanisms of gelatinase expression.

SEVh exposure favors migratory morphology of MDA-MB-231 cells in normoxia

Upon visual interpretation, cell morphology was modified slightly by SEVh treatment in all conditions, particularly on Matrigel coating (Figure 4a). Untreated cells in normoxia have a distinct F-actin arrangement, with parallel fibers crossing the cytoplasm on its axis. This pattern is disrupted by hypoxia and/or SEVh, which generates a specific F-actin arrangement alongside the cellular perimeter. The same behavior is visible in uncoated and gelatin-coated groups (data not shown). An interesting feature of SEVh signaling in normoxia is the development of invadopodia, F-actin-rich protuberances displayed throughout the periphery of cells [38] (Figure 4b).

Overall, cell circularity decreased after exposure to collagen-based matrices for 24 and 48 h (Figures 4c-e). In uncoated surfaces, SEVh treatment in hypoxia and normoxia increased circularity of cells compared to their respective controls in both timepoints (Figure 4c). When collagen-based matrices were used, this behavior changed: after 24 h, SEVh-treated normoxic cells were 32% more elongated in gelatin than the untreated control (Figure 4d), and 58% more elongated in Matrigel (Figure 4e). For comparison, cell circularity was not altered by hypoxia alone, and only changed after 24h exposure to SEVh

 doi:10.20944/preprints202208.0462.v1

in hypoxia when cells were adhered to Matrigel (Figure 4e). Considering that increased circularities may be resulting from cell stress, our results suggest that any type of collagen-based ECM is essential for the development of an elongated phenotype in TNBC.

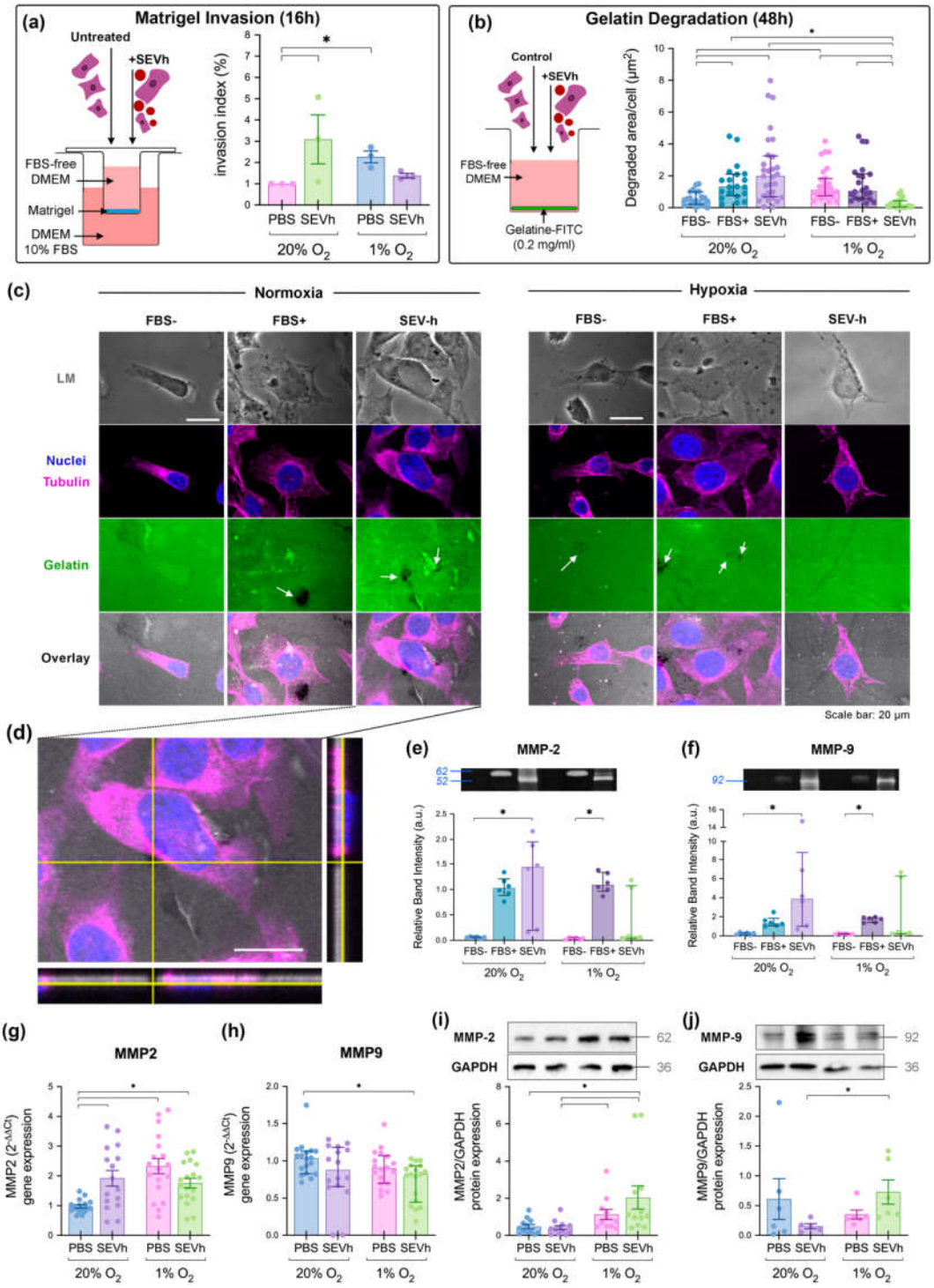

Figure 3. Normoxia triggers SEVh-mediated long-term invasion (a) Experimental diagram of Matrigel invasion chamber assay (left) and invasion index (%) after 16h (median ± interquartile, right). (b) Experimental diagram of fluorescent gelatin degradation assay (left) and comparison of the degraded area after 48 h (median ± interquartile, right). (c) Representative images of gelatin degradation assay in light microscopy (LM), and fluorescent nuclei (DAPI, blue), tubulin (AlexaFluor647, pink) and gelatin (0.2 mg/ml, fluorescein, green). Below, merged images.

Preprints (www.preprints.org) | NOT PEER-REVIEWED | Posted: 26 August 2022 doi:10.20944/preprints202208.0462.v1

Degradation spots in black are indicated by white arrows (scale bar: 20 μm) (d) Orthogonal view of normoxic, SEVh-treated cells with degradation spot near the cellular body (scale bar: 20 μm). (e-f) Proteolytic activity from gelatin degradation assay supernatant of (e) MMP-2 (mean ± SEM) and (f) MMP-9 (median ± interquartile). (g-h) Gene expression of (g) MMP2 (mean ± SEM) and (h) MMP9 (median ± interquartile) in MDA-MB-231 cells. (i-j) Protein expression of (i) MMP-2 (mean ± SD) and (j) MMP-9 (median ± interquartile). *p<0.05

Since there is an inherent phenotypical diversity of MDA-MB-231 cells, which morphs according to matrix stiffness and function [37], cell circularity should not be the only parameter to compare cell phenotypes. Hence, to confirm a migratory morphology, we cross-referenced circularity results with auxiliary parameters of AR and perimeter/area (Figure S3a-f). Matrigel-adhered SEVh-treated normoxic cells had higher AR and perimeter/area values, indicating lengthier cells and confirming a migratory phenotype.

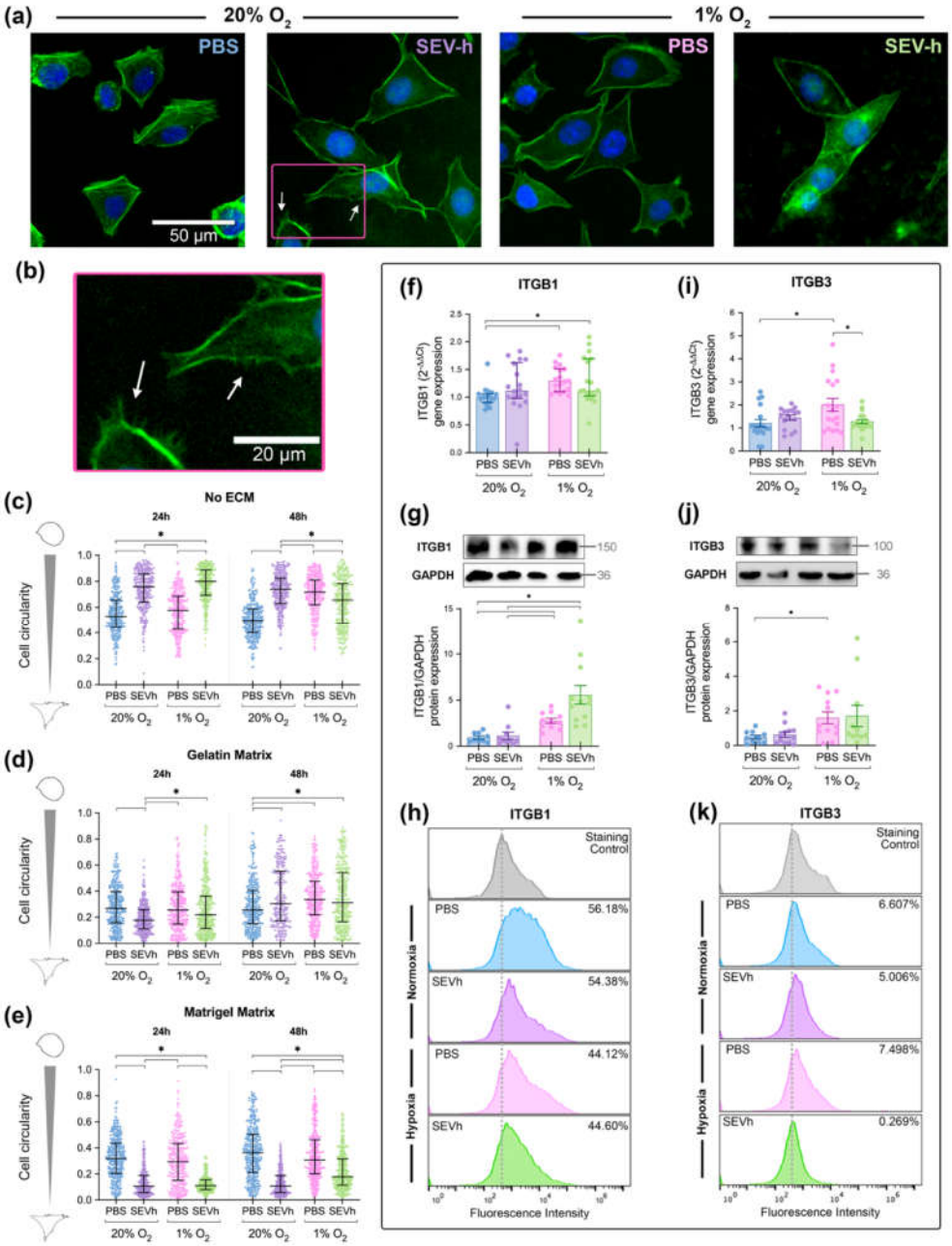

 doi:10.20944/preprints202208.0462.v1

Figure 4. Phenotypical alterations promoted by hypoxia and/or SEVh exposure (a) Representative images of untreated (PBS) and treated (SEVh) MDA-MB-231 cells in matrigel matrix, following a 24h incubation in normoxia (20% O_2) or hypoxia (1% O_2). White arrows indicate the presence of invadopodia, indicating a migratory phenotype (scalebar: 50 μm). (b) Detailed vision of invadopodia in normoxic cells following SEVh exposure (scalebar: 20 μm). (c-e) Circularity determination after 24h and 48h, of cells plated atop (c) uncoated surface, (d) gelatin (0.2 mg/ml) matrix and (e) Matrigel matrix (1:1, v/v). (f) Gene expression (median ± interquartile), (g) whole cell protein expression (mean ± SEM), and (h) surface protein expression of integrin subunit β1 (data presented as mean % of triplicates of two independent assays). (i) Gene expression (mean ± SEM), (j) whole cell protein expression (mean ± SEM), and (k) surface protein expression of integrin subunit β3 (data presented as mean % of triplicates of two independent assays). *p<0.05

Hypoxia interferes with β1 and β3 integrin subunit expression in TNBC cells

SEVh treatment did not alter gene and protein expression of integrin subunits β1 and β3, which regulate migration and invasion [39]. On the other hand, hypoxia appeared to be a keen regulator for integrin subunit β1. Hypoxia significantly upregulated gene expression (Figure 4f) and protein expression in whole cell lysates (Figure 4g). However, when probing for peripheric integrin levels via flow cytometry, we found that surface-available β1 was diminished in hypoxia (Figure 4h).

The same promoting effect of hypoxia towards integrin gene and protein expression was found for β3 subunit; however, there was no downregulation of surface-available β3 integrin (Figure 4i-k). Although SEVh signaling did not interfere with integrin β3 expression in normoxia, it decreased gene expression by 36.3% in hypoxia (Figure 4i). Interestingly, it did not alter protein levels on whole cell lysates (Figure 4j), but dwindled surface-available β3 to basal levels (Figure 4k).

Hypoxia-derived apoptosis is modulated by SEVh signaling

The management of cell death by either apoptosis, necrosis, autophagy or other processes in hypoxia is an established response to hypoxia [40], which we have corroborated. The exposure of cells to 1% O_2 atmosphere increased late apoptosis percentage when compared to the untreated normoxic control (Figure 5a,b). Other parameters analyzed (early apoptosis, live and dead cells) were unchanged between groups. Focusing on SEVh signaling, the lack of statistically relevant differences in cell fate under both oxygen settings indicates that SEVh (1) aids the modulation of hypoxia-derived apoptosis response; and (2) does not promote cell death in normoxic cells.

Hypoxic cells regulate apoptosis via the HIF pathway, whose main component (HIF-1) controls the balance between pro- and anti-apoptotic signals [41]. HIF-1 is a heterodimer formed when an α subunit evades ubiquitin degradation and assembles with a β subunit [41]. Our findings indicate that HIF-1α gene expression is diminished in MDA-MB-231 cells in hypoxia, regardless of SEVh exposure (Figure 5c). Although not statistically relevant, we also saw a tendency for decreased HIF-1α gene expression after SEVh signaling, especially in hypoxia (p = 0.07). Its protein levels followed the same pattern from gene expression analysis, but with a significant increase in HIF-1α in SEVh-treated hypoxic cells (Figure 5d). The paradoxical result in this group may suggest that SEVh is also interfering on the regulatory mechanism of HIF-1α when oxidative stress is established.

MDA-MB-231 comparative proteome shows that SEVh favors a shift in cytoskeleton arrangements and cell cycle in normoxia

Label-free proteomic analysis of cells exposed to SEVh, under normoxia and hypoxia conditions, showed a distinct proteome profile for each group. 2615 proteins were detected overall, with 1441 shared among all groups. We found 11 proteins exclusive to normoxic groups and 124 in hypoxia, with 196 unique proteins in untreated cells in normoxia (PBS-N), 18 in SEVh-treated cells in normoxia (SEVh-N), 108 in untreated cells

 doi:10.20944/preprints202208.0462.v1

in hypoxia (PBS-H) and 120 in SEVh-treated cells in hypoxia (SEVh-H). Shared proteins between groups are described at the Venn's diagram in Figure 6a. Principal component analysis (PCA) clustered replicates according to their determinant characteristics (Figure 6b). PC values correspond to 36.0%, 20.7%, 11.8%, 10.2% and 4.8% of designated variance.

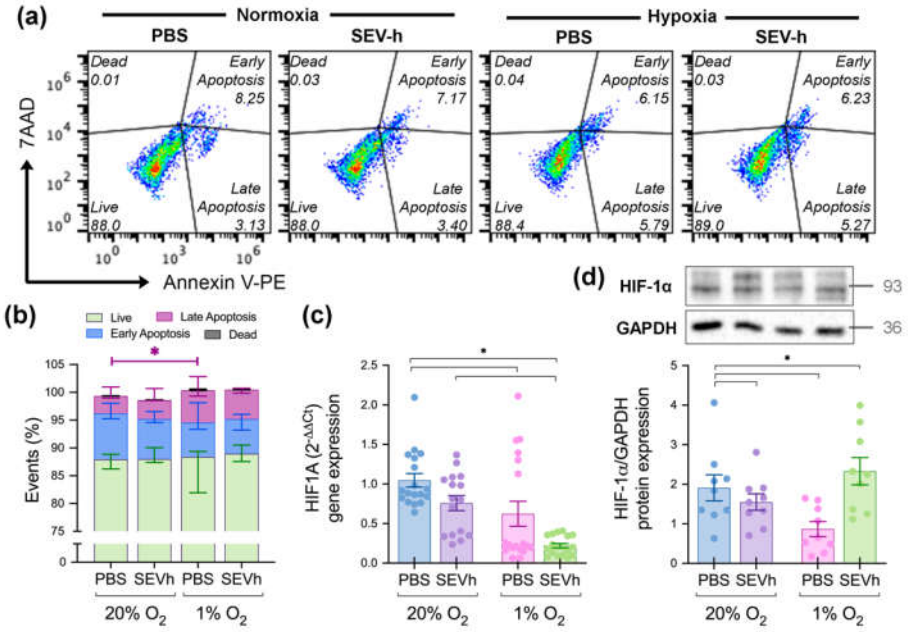

Figure 5. HIF-dependent cell responses resulted from SEVh treatment (a) Scatter plot of apoptosis assay; population (%) displayed as average of two independent assays in technical triplicates. (b) Comparative graph of the four possible outcomes for cells (live, early apoptotic, late apoptotic or dead) as determined by the apoptosis assay. Statistical significance obtained from early apoptotic cells between untreated groups (normoxia x hypoxia), as indicated in the fuchsia bar above (c-d) Levels of HIF-1α (c) gene expression (mean ± SEM) and (d) whole cell protein expression (mean ± SEM) (*p<0.05)

Univariate statistical analysis identified 105 proteins with differential expression between all four groups (p<0.05), with 62 most divergent proteins (p<0.01, Figure 6c, Table S2). Pairwise comparisons detected 79 distinct proteins between untreated cells in normoxia versus hypoxia (PBS-N vs. PBS-H), 66 for SEVh-treated cells in normoxia versus hypoxia (SEVh-N vs. SEVh-H), 18 for untreated versus SEVh-treated cells in normoxia (PBS-N vs. SEVh-N), 42 for untreated versus SEVh-treated cells in hypoxia (PBS-H vs. SEVh-H) and 80 for untreated, normoxic cells versus SEVh-treated, hypoxia cells (PBS-N vs. SEVh-H). The top 62 divergent protein abundance values are displayed at Figure 6d, and the interaction diagram of all statistically distinct proteins is in Figure 6e.

SEVh directly interferes with the proteome of cells in normoxia, especially with the upregulation of γ-tubulin complex binding by TUBGCP6, TUBG1, TUBGCP3 and TUBGCP2 (FDR: 9.7×10^{-6}), hence increasing microtubule nucleation (FDR: 2.6×10^{-4}), and protein polymerization (FDR: 3.3×10^{-4}). Other additional pathways induced by SEVh signaling include mitochondrial biogenesis, citric acid cycle and synthesis of ubiquitin E1 and E2 enzymes (FDR: 1.71×10^{-1}). All together, these results indicate that SEVh signaling in normoxia promotes substantial alterations in cell metabolism, favoring the cell cycle and survival of tumoral cells.

In hypoxia, SEVh treatment led to distinct responses, favoring response to stress (KEAP1, RBX1, POLR2C, POLR2I, ADD1, SETD7, NPLOC4, NCCRP1, UCHL5, CTH, BAG6, HSPA2, AK4, C4orf27 and POLR2E; FDR: 1.82×10^{-2}) and other metabolic processes (FDR: 2.39×10^{-2}). Particularly, it led to an increase in mRNA biogenesis and splicing (PQBP1, POLR2C, POLR2I, DDX23 and POLR2E), DNA repair (RBX1, POLR2C, POLR2I,

Preprints (www.preprints.org) | NOT PEER-REVIEWED | Posted: 26 August 2022 doi:10.20944/preprints202208.0462.v1

NPLOC4 and POLR2E) and degradation of cysteine and homocysteine (FDR: $8.04x10^{-2}$). Overall, these results reveal an oxygen-dependent modulation for SEVh signaling in tumoral cells, generating distinct survival mechanisms.

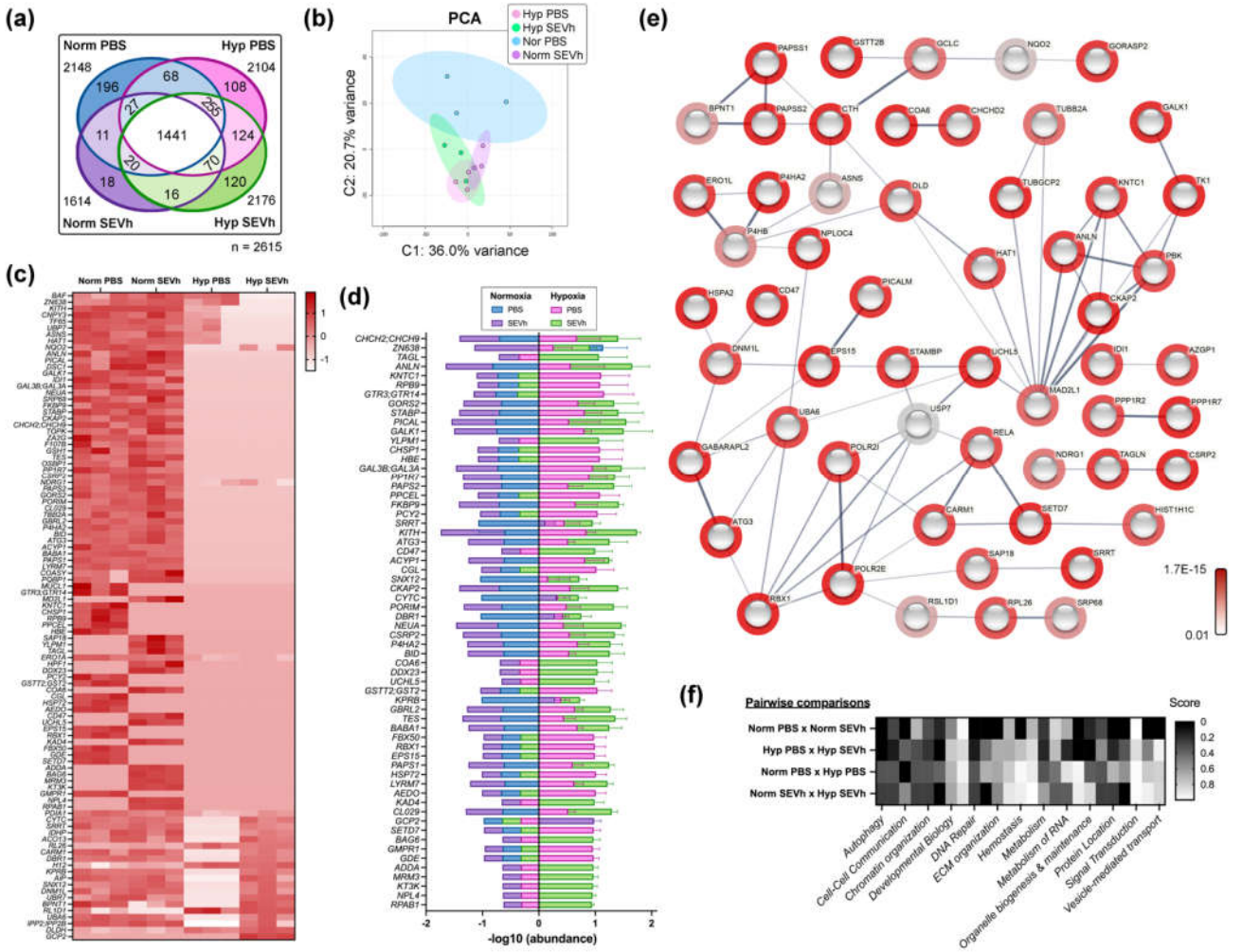

Figure 6. Comparative proteome analysis (a) Venn's diagram of protein distribution in MDA-MB-231, noting cells incubated in normoxia (Norm) or hypoxia (Hyp) in the presence or absence of SEVh (b) Principal component analysis (PCA) scores plot (c) Heatmap of 105 proteins differentially expressed in cells treated or nor with SEVh, in normoxia and hypoxia (p<0.05) (d) Values of -$\log_{10}$ (abundance) of 62 most divergent proteins differently expressed between groups (p<0.01) (e) Interaction map of all differentially expressed proteins in cellular samples with hidden disconnected nodes, created at String-DB. Halos indicate the strength of p values from the statistical analysis of normalized data (red to gray – scale below). Strings shown as confidence network edges, with soft lines for medium confidence (0.4), regular lines for high confidence (0.7) and bold lines for highest confidence (0.9) (d) Heatmap containing the enrichment analysis of statistically distinct proteins by pairwise comparisons, developed in Reactome. Upregulated pathways are indicated below, with significance varying from most (black) to least (white) enriched in each comparison, following the scale (left - p<0.05).

Hypoxia alone also interferes with cell metabolism, increasing particularly the catabolic activity of both SEVh-treated ($6.9x10^{-3}$) and untreated cells ($6.02x10^{-3}$) and response to stress of the control groups ($3.34x10^{-1}$). Although programmed cell death, a staple of hypoxia signaling, was slightly favored by our proteomic analysis, our results also show an increase in autophagy (FDR: $3.34x10^{-1}$ for untreated groups; $2.5x10^{-1}$ for SEVh-treated groups). Akin to the literature, several proteins from hypoxic cells are

 doi:10.20944/preprints202208.0462.v1

related to DNA damage and repair, including USP7, BABAM1, RBX1 and POLR2I ($3.34x10^{-1}$). On the other hand, SEVh signaling induces major mitochondrial and proteolytic pathways in hypoxia when compared to normoxia, such as the transport and synthesis of PAPS ($8.99x10^{-2}$) and metalloprotease deubiquitinating enzymes (DUBs) ($2.05x10^{-1}$). Details of enriched biological pathways may be found at Figure 6f.

4. Discussion

Cell invasion is a multi-step process critical for the metastatic cascade since it allows cells to detach from the primary tumor and seek a new niche for development [42]. It can be triggered by several factors, such as intratumoral hypoxia, whose establishment is a direct result of increased proliferative rates and nutrient consumption [43]. While hypoxia alone is crucial for eliciting pro-tumoral responses, here we demonstrated that its derived SEV may also contribute to tumor progression and invasive response in TNBC cells, particularly under oxygen-rich settings.

The overall distinct pattern of responses found between SEVh-treated TNBC cells in hypoxia and normoxia denotes the importance of oxygen-dependent responses in cancer, affecting specifically the HIF-1 pathway. In healthy tissues, HIF-1 is hydroxylated at a conserved proline residue, which is a mark for proteasomal degradation; however, in hypoxia, reactive oxygen species (ROS) inhibit prolyl-hydroxylase domain enzymes (PHDs) from cleaving this residue, thus enabling the binding of HIF subunits to form a transcriptional regulator that interferes in metabolism, redox homeostasis, angiogenesis, tumorigenesis, and inflammation [44]. Our results hint at HIF-1α degradation, considering both the diminished protein expression of HIF-1α and the enrichment in ubiquitination on normoxic cells after SEVh exposure. HIF-1α gene expression was also decreased in hypoxia, thus favoring a negative feedback loop on the HIF-1 pathway. These results denote that, although SEVh exposure and/or hypoxia directly interfere with the HIF-1 pathway, the singular presence of SEVh may trigger HIF-dependent responses in normoxic TNBC cells.

HIF-1 activation promotes pro-tumoral responses such as ECM remodeling – either by inducing ECM protein secretion [45] or controlling MMP expression [46]. Our findings show a distinct modulation of gelatinase expression by hypoxia and/or SEVh signaling; while MMP-2 expression and activity were significantly upregulated, a lesser expressive MMP-9 downregulation was observed. This balanced response may occur due to their shared, yet distinct, activation pathway via MMP-1. MMP-1 is a collagenase with direct connections to NF-κB signaling that participates on the canonical activation of MMP-9 [47] and on one of the less effective, non-canonical activation pathways of MMP-2 [47]. Considering that MMP-9 can be inhibited by TIMP-1, which is favored by HIF signaling and has been previously linked to triggering pro-metastatic behavior alongside miR-210, we propose MMP-2 activation may be preferred over MMP-9 whenever hypoxia is present – either via their EVs or by direct oxygen stress [48].

ECM remodeling interferes directly with the expression pattern of integrins, cellular adhesion receptors that mediate outside-in and inside-out responses [39]. Integrin profiling in cancer cells differ based on tumor aggressiveness, cellular origin and tumoral progression [49], and this profile can be passed onto extracellular vesicles [50], thus aiding vesicular trafficking [51], organotropism [10] and metastasis [52]. β1 and β3 integrin subunits are often upregulated in cancer and linked to responses of cell motility [53], adhesion [54], invasion [55,56] and angiogenesis [57,58]; hence, we investigated whether they are affected by SEVh exposure. We found that a hypoxic atmosphere, instead of the signaling from SEVh, modulates gene and protein expression of β1 and β3 integrins; however, the availability of these integrins to the cell surface in hypoxia differs in the presence of SEVh. We suggest that SEVh signaling regulates integrin trafficking pathways, preventing certain subunits, such as integrin β3, from reaching the cell surface in low oxygen settings.

 doi:10.20944/preprints202208.0462.v1

Integrin differential expression and availability impact directly on cellular morphology. The cytoplasmic tail of the β subunit is linked to F-actin via talin-1, therefore when the extracellular segment binds to ECM components, molecular clutches are formed to propel the cell onwards, thus creating a leading edge and promoting a migratory phenotype [15,39,59]. TNBC cells display a plethora of phenotypes based on ECM composition and stiffness [60], as observed on our morphological analysis, where the three complementary parameters identified several possibilities for cell phenotype. In a complex ECM setting (i.e., Matrigel), we observed that SEVh exposure under normoxia led to low circularity and higher elongation in TNBC cells, which is consistent to a migratory phenotype. This, coupled with the identification of invadopodia - F-actin-rich protrusion on the cellular edge [38] - and the results obtained from both *in vitro* invasion assays, indicate that an invasive phenotype is favored in TNBC cells by SEVh signaling whenever advantageous conditions of oxygen and matrix composition are found.

We unveiled the baseline pathways and proteins favored by SEVh signaling and/or hypoxia in MDA-MB-231 cells plated in uncoated settings, which may differ from investigations in which cells are adhered to ECM components. We found that (1) each group presented a distinct protein and pathway enrichment, and (2) the proteome of SEVh-treated groups diverged from the raw proteome of SEVh, which indicates a likely internalization of these particles to elicit cellular responses. In particular, the activation of survival pathways and modulation of the cell cycle by SEVh in normoxia, and the increase in proteolysis and DNA damage in hypoxia, confirm how oxygenation is important for determining cell fate whenever SEVh signaling is available. While the proteomes of both TNBC cell line MDA-MB-231 [61] and its derived EVs [11] are well known, and an in-depth investigation towards the effects of mild (1.2% O_2) and harsh (0.2% O_2) hypoxia was recently published [62], here we demonstrate for the first time how SEV derived from hypoxic TNBC cells modify the proteome of their originating cells in two oxygen settings (normoxia and hypoxia), while also characterizing the proteome of said SEVh and distinguishing it from their normoxic counterparts.

Lastly, it is important to denote that our experimental design introduced TNBC cells to a 1% oxygen atmosphere right after plating, which is distinct from most literature findings, who either vary the oxygen ratio from 0.1 up to 5% [4,62–65], submit cells to chemical hypoxia [66] or incubate adhered cells to a hypoxic atmosphere [5,8,43]. Therefore, it is logical that some responses are slightly divergent from the ones found in the literature, including integrin [67] and HIF-1α [68] profiling, yet others – such as increased SEV yield [7], apoptosis [69] and cell invasion [8], are persistent. Nevertheless, this is the first study that explains how self-signaling of SEVh to hypoxic TNBC cells lead to important intracellular modifications, including increased proteolysis, catabolism and, overall, a severe response to hypoxic stress.

5. Conclusion

SEV separated from TNBC cell line MDA-MB-231 in hypoxia promotes invasive behaviors in normoxia, while inducing proteolytic and catabolic pathways in hypoxia. Cell invasion is favored by SEVh under advantageous conditions of oxygen and matrix composition, due to the modulation of gelatinase (i.e., MMP-2 and MMP-9) and integrin (i.e., subunits β1 and β3) expression and availability. These modifications interfere with the F-actin cytoskeleton, to create a migratory phenotype coupled with invadopodia development. Protein profiling of SEVh-treated, normoxic cells indicate a baseline favoring metabolic processes and cell cycle, modulating cell health away from apoptotic pathways that are enriched in hypoxia. Overall, our results demonstrate the importance of hypoxic signaling via SEV in a tumoral setting for the establishment of metastasis.

Supplementary Materials: The following supporting information can be downloaded at: www.mdpi.com/xxx/s1, Figure S1: Additional methodological details; Figure S2: Cell invasion in acute hypoxia; Figure S3: Migratory morphology is induced by SEVh in Matrigel; Table S1:

Differential proteomic profile of SEVh (p<0.01); Table S2: Differential proteomic profile of MDA-MB-231 cells exposed to normoxia or hypoxia, with or without SEVh treatment (p<0.05).

Author Contributions: Conceptualization, Bianca Pachane, Heloisa Selistre-de-Araujo and Wanessa Altei; Data curation, Bianca Pachane and Thais Cataldi; Formal analysis, Bianca Pachane and Wanessa Altei; Funding acquisition, Bianca Pachane, Carlos Labate, Heloisa Selistre-de-Araujo and Wanessa Altei; Investigation, Bianca Pachane, Ana Carolina Nunes, Thais Cataldi, Kelli Micocci, Bianca Moreira and Wanessa Altei; Methodology, Bianca Pachane, Thais Cataldi, Kelli Micocci, Bianca Moreira, Heloisa Selistre-de-Araujo and Wanessa Altei; Project administration, Bianca Pachane; Resources, Carlos Labate, Heloisa Selistre-de-Araujo and Wanessa Altei; Software, Bianca Pachane, Carlos Labate and Heloisa Selistre-de-Araujo; Supervision, Heloisa Selistre-de-Araujo and Wanessa Altei; Validation, Bianca Pachane, Ana Carolina Nunes, Thais Cataldi and Kelli Micocci; Visualization, Carlos Labate; Writing – original draft, Bianca Pachane, Heloisa Selistre-de-Araujo and Wanessa Altei; Writing – review & editing, Ana Carolina Nunes, Thais Cataldi, Kelli Micocci and Bianca Moreira. All authors have read and agreed to the published version of the manuscript.

Funding: This work was supported by the São Paulo Research Foundation (FAPESP) under Grants 2021/01983-4, 2019/05149-9, 2019/11437-7, 2019/17737-2 and 2017/06198-8; Coordenação de Aperfeiçoamento de Pessoal de Nível Superior (CAPES), code 001 and Conselho Nacional de Desenvolvimento Científico e Tecnológico (CNPq) under Grant 429235/2018-6.

Institutional Review Board Statement: Not applicable.

Informed Consent Statement: Not applicable.

Data Availability Statement: Detailed experimental data for EV isolation and characterization is available on the EV-TRACK platform[32] (EV-TRACK ID: EV220177). Data are available via ProteomeXchange with identifier PXD035244. Raw data from other assays is available on demand.

Acknowledgments: The authors thank all Biochemistry and Molecular Biology Laboratory members for critical advice and proof-reading of the manuscript. We thank the Proteomic, Lipidomic and Metabolomic Multiuser Laboratory (ESALQ/USP) for services and facilities. We thank Professors Marcia Cominetti (LABEN/UFSCar) for MMP-9 antibody donation; the Laboratory of Structural Characterization (LCE/DEMa/UFSCar) for the electron microscopy facilities; Professors Otavio Thiemann and Glaucius Oliva (IFSC/USP) for Beckman ultracentrifuge and rotors; Professors Maria Palmira Gremião and Marlus Chorilli (FCFAR/UNESP) and Eneida de Paula (IB/UNICAMP) for use of Nanosight NS300. Graphical abstract was created using BioRender.com.

Conflicts of Interest: The authors declare no conflict of interest. The funders had no role in the design of the study; in the collection, analyses, or interpretation of data; in the writing of the manuscript; or in the decision to publish the results.

References

1. Kumar, A.; Deep, G. Hypoxia in Tumor Microenvironment Regulates Exosome Biogenesis: Molecular Mechanisms and Translational Opportunities. *Cancer Letters* **2020**, *479*, 23–30, doi:10.1016/j.canlet.2020.03.017.
2. McAleese, C.E.; Choudhury, C.; Butcher, N.J.; Minchin, R.F. Hypoxia-Mediated Drug Resistance in Breast Cancers. *Cancer Letters* 2021, *502*, 189–199.
3. Ebright, R.Y.; Zachariah, M.A.; Micalizzi, D.S.; Wittner, B.S.; Niederhoffer, K.L.; Nieman, L.T.; Chirn, B.; Wiley, D.F.; Wesley, B.; Shaw, B.; et al. HIF1A Signaling Selectively Supports Proliferation of Breast Cancer in the Brain. *Nature Communications* **2020**, *11*, doi:10.1038/s41467-020-20144-w.
4. Hoffmann, C.; Mao, X.; Brown-Clay, J.; Moreau, F.; al Absi, A.; Wurzer, H.; Sousa, B.; Schmitt, F.; Berchem, G.; Janji, B.; et al. Hypoxia Promotes Breast Cancer Cell Invasion through HIF-1α-Mediated up-Regulation of the Invadopodial Actin Bundling Protein CSRP2. *Scientific Reports* **2018**, *8*, 1–14, doi:10.1038/s41598-018-28637-x.
5. Xie, J.; Xiao, Y.; Zhu, X. yan; Ning, Z. yu; Xu, H. fan; Wu, H. min Hypoxia Regulates Stemness of Breast Cancer MDA-MB-231 Cells. *Medical Oncology* **2016**, *33*, 1–7, doi:10.1007/s12032-016-0755-7.
6. Begg, K.; Tavassoli, M. Inside the Hypoxic Tumour: Reprogramming of the DDR and Radioresistance. *Cell Death Discovery* **2020**, *6*, doi:10.1038/s41420-020-00311-0.

7. King, H.W.; Michael, M.Z.; Gleadle, J.M. Hypoxic Enhancement of Exosome Release by Breast Cancer Cells. *BMC Cancer* **2012**, *12*, 10.
8. Wang, T.; Gilkes, D.M.; Takano, N.; Xiang, L.; Luo, W.; Bishop, C.J.; Chaturvedi, P.; Green, J.J.; Semenza, G.L. Hypoxia-Inducible Factors and RAB22A Mediate Formation of Microvesicles That Stimulate Breast Cancer Invasion and Metastasis. *Proceedings of the National Academy of Sciences* **2014**, *111*, E3234–E3242, doi:10.1073/pnas.1410041111.
9. Foulkes, W.D.; Smith, I.E.; Reis-Filho, J.S. Triple-Negative Breast Cancer. *New England Journal of Medicine* **2010**, *363*, 1938–1948, doi:10.1056/NEJMra1001389.
10. Hoshino, A.; Costa-Silva, B.; Shen, T.-L.; Rodrigues, G.; Hashimoto, A.; Tesic Mark, M.; Molina, H.; Kohsaka, S.; di Giannatale, A.; Ceder, S.; et al. Tumour Exosome Integrins Determine Organotropic Metastasis. *Nature* **2015**, *527*, 329–335, doi:10.1038/nature15756.
11. Palazzolo, G.; Albanese, N.N.; di Cara, G.; Gygax, D.; Vittorelli, M.L.; Pucci-Minafra, I. Proteomic Analysis of Exosome-like Vesicles Derived from Breast Cancer Cells. *Anticancer Research* **2012**, *32*, 847–860, doi:32/3/847 [pii].
12. Muz, B.; de la Puente, P.; Azab, F.; Azab, A.K. The Role of Hypoxia in Cancer Progression, Angiogenesis, Metastasis, and Resistance to Therapy. *Hypoxia* **2015**, 83, doi:10.2147/hp.s93413.
13. Bister, N.; Pistono, C.; Huremagic, B.; Jolkkonen, J.; Giugno, R.; Malm, T. Hypoxia and Extracellular Vesicles: A Review on Methods, Vesicular Cargo and Functions. *Journal of Extracellular Vesicles* 2020, *10*.
14. Yousefi, H.; Vatanmakanian, M.; Mahdiannasser, M.; Mashouri, L.; Alahari, N. v.; Monjezi, M.R.; Ilbeigi, S.; Alahari, S.K. Understanding the Role of Integrins in Breast Cancer Invasion, Metastasis, Angiogenesis, and Drug Resistance. *Oncogene* **2021**, doi:10.1038/s41388-020-01588-2.
15. Friedl, P.; Alexander, S. Cancer Invasion and the Microenvironment: Plasticity and Reciprocity. *Cell* **2011**, *147*, 992–1009, doi:10.1016/j.cell.2011.11.016.
16. Schoumacher, M.; Goldman, R.D.; Louvard, D.; Vignjevic, D.M. Actin, Microtubules, and Vimentin Intermediate Filaments Cooperate for Elongation of Invadopodia. *Journal of Cell Biology* **2010**, *189*, 541–556, doi:10.1083/jcb.200909113.
17. Hoshino, D.; Kirkbride, K.C.; Costello, K.; Clark, E.S.; Sinha, S.; Grega-Larson, N.; Tyska, M.J.; Weaver, A.M. Exosome Secretion Is Enhanced by Invadopodia and Drives Invasive Behavior. *Cell Reports* **2013**, *5*, 1159–1168, doi:10.1016/j.celrep.2013.10.050.
18. Théry, C.; Amigorena, S.; Raposo, G.; Clayton, A. Isolation and Characterization of Exosomes from Cell Culture Supernatants and Biological Fluids. *Current Protocols in Cell Biology* **2006**, *30*, 3.22.1-3.22.29, doi:10.1002/0471143030.cb0322s30.
19. Schindelin, J.; Arganda-Carrera, I.; Frise, E.; Verena, K.; Mark, L.; Tobias, P.; Stephan, P.; Curtis, R.; Stephan, S.; Benjamin, S.; et al. Fiji - an Open Platform for Biological Image Analysis. *Nature Methods* **2009**, *9*, doi:10.1038/nmeth.2019.Fiji.
20. Meier, F.; Brunner, A.D.; Koch, S.; Koch, H.; Lubeck, M.; Krause, M.; Goedecke, N.; Decker, J.; Kosinski, T.; Park, M.A.; et al. Online Parallel Accumulation–Serial Fragmentation (PASEF) with a Novel Trapped Ion Mobility Mass Spectrometer. *Molecular and Cellular Proteomics* **2018**, *17*, 2534–2545, doi:10.1074/mcp.TIR118.000900.
21. Meier, F.; Beck, S.; Grassl, N.; Lubeck, M.; Park, M.A.; Raether, O.; Mann, M. Parallel Accumulation-Serial Fragmentation (PASEF): Multiplying Sequencing Speed and Sensitivity by Synchronized Scans in a Trapped Ion Mobility Device. *Journal of Proteome Research* **2015**, *14*, 5378–5387, doi:10.1021/acs.jproteome.5b00932.
22. Bateman, A. UniProt: A Worldwide Hub of Protein Knowledge. *Nucleic Acids Research* **2019**, *47*, D506–D515, doi:10.1093/nar/gky1049.

23. Tyanova, S.; Temu, T.; Cox, J. The MaxQuant Computational Platform for Mass Spectrometry-Based Shotgun Proteomics. *Nature Protocols* **2016**, *11*, 2301–2319, doi:10.1038/nprot.2016.136.
24. Tyanova, S.; Temu, T.; Sinitcyn, P.; Carlson, A.; Hein, M.Y.; Geiger, T.; Mann, M.; Cox, J. The Perseus Computational Platform for Comprehensive Analysis of (Prote)Omics Data. *Nature Methods* 2016, *13*, 731–740.
25. Pang, Z.; Chong, J.; Zhou, G.; de Lima Morais, D.A.; Chang, L.; Barrette, M.; Gauthier, C.; Jacques, P.É.; Li, S.; Xia, J. MetaboAnalyst 5.0: Narrowing the Gap between Raw Spectra and Functional Insights. *Nucleic Acids Research* **2021**, *49*, W388–W396, doi:10.1093/nar/gkab382.
26. Szklarczyk, D.; Gable, A.L.; Nastou, K.C.; Lyon, D.; Kirsch, R.; Pyysalo, S.; Doncheva, N.T.; Legeay, M.; Fang, T.; Bork, P.; et al. The STRING Database in 2021: Customizable Protein-Protein Networks, and Functional Characterization of User-Uploaded Gene/Measurement Sets. *Nucleic Acids Research* **2021**, *49*, D605–D612, doi:10.1093/nar/gkaa1074.
27. Griss, J.; Viteri, G.; Sidiropoulos, K.; Nguyen, V.; Fabregat, A.; Hermjakob, H. ReactomeGSA - Efficient Multi-Omics Comparative Pathway Analysis. *Molecular and Cellular Proteomics* **2020**, *19*, 2115–2124, doi:10.1074/mcp.TIR120.002155.
28. Perez-Riverol, Y.; Csordas, A.; Bai, J.; Bernal-Llinares, M.; Hewapathirana, S.; Kundu, D.J.; Inuganti, A.; Griss, J.; Mayer, G.; Eisenacher, M.; et al. The PRIDE Database and Related Tools and Resources in 2019: Improving Support for Quantification Data. *Nucleic Acids Research* **2019**, *47*, D442–D450, doi:10.1093/nar/gky1106.
29. Leber, T.M.; Balkwill, F.R. Zymography: A Single-Step Staining Method for Quantitation of Proteolytic Activity on Substrate Gels. *Analytical Biochemistry* **1997**, *249*, 24–28, doi:10.1006/abio.1997.2170.
30. Livak, K.J.; Schmittgen, T.D. Analysis of Relative Gene Expression Data Using Real-Time Quantitative PCR and the 2-ΔΔCT Method. *Methods* **2001**, *25*, 402–408, doi:10.1006/meth.2001.1262.
31. Théry, C.; Witwer, K.W.; Aikawa, E.; Alcaraz, M.J.; Anderson, J.D.; Andriantsitohaina, R.; Antoniou, A.; Arab, T.; Archer, F.; Atkin-Smith, G.K.; et al. Minimal Information for Studies of Extracellular Vesicles 2018 (MISEV2018): A Position Statement of the International Society for Extracellular Vesicles and Update of the MISEV2014 Guidelines. *Journal of Extracellular Vesicles* **2018**, *7*, doi:10.1080/20013078.2018.1535750.
32. van Deun, J.; Mestdagh, P.; Agostinis, P.; Akay, Ö.; Anand, S.; Anckaert, J.; Martinez, Z.A.; Baetens, T.; Beghein, E.; Bertier, L.; et al. EV-TRACK: Transparent Reporting and Centralizing Knowledge in Extracellular Vesicle Research. *Nature Methods* 2017, *14*, 228–232.
33. Hermann, M.R.; Jakobson, M.; Colo, G.P.; Rognoni, E.; Jakobson, M.; Kupatt, C.; Posern, G.; Fässler, R. Integrins Synergise to Induce Expression of the MRTF-A-SRF Target Gene ISG15 for Promoting Cancer Cell Invasion. *Journal of Cell Science* **2016**, *129*, 1391–1403, doi:10.1242/jcs.177592.
34. Mossmann, D.; Park, S.; Hall, M.N. MTOR Signalling and Cellular Metabolism Are Mutual Determinants in Cancer. *Nature Reviews Cancer* 2018, *18*, 744–757.
35. Derynck, R.; Zhang, Y.E. *Smad-Dependent and Smad-Independent Pathways in TGF-b Family Signalling*; 2003;
36. Gaudet, P.; Livstone, M.S.; Lewis, S.E.; Thomas, P.D. Phylogenetic-Based Propagation of Functional Annotations within the Gene Ontology Consortium. *Briefings in Bioinformatics* **2011**, *12*, 449–462, doi:10.1093/bib/bbr042.
37. Zhang, X.; Chan, T.; Mak, M. Morphodynamic Signatures of MDA-MB-231 Single Cells and Cell Doublets Undergoing Invasion in Confined Microenvironments. *Scientific Reports* **2021**, *11*, doi:10.1038/s41598-021-85640-5.
38. Om Alblazi, K.M.; Siar, C.H. Cellular Protrusions - Lamellipodia, Filopodia, Invadopodia and Podosomes - and Their Roles in Progression of Orofacial Tumours: Current Understanding. *Asian Pacific Journal of Cancer Prevention* **2015**, *16*, 2187–2191, doi:10.7314/APJCP.2015.16.6.2187.

39. Hamidi, H.; Ivaska, J. Every Step of the Way: Integrins in Cancer Progression and Metastasis. *Nature Reviews Cancer* **2018**, *18*, 533–548, doi:10.1038/s41568-018-0038-z.
40. Qiu, Y.; Li, P.; Ji, C. Cell Death Conversion under Hypoxic Condition in Tumor Development and Therapy. *International Journal of Molecular Sciences* 2015, *16*, 25536–25551.
41. Greijer, A.E.; van der Wall, E. The Role of Hypoxia Inducible Factor 1 (HIF-1) in Hypoxia Induced Apoptosis. *Journal of Clinical Pathology* 2004, *57*, 1009–1014.
42. Chambers, A.F.; Werb, Z. Invasion and Metastasis—Recent Advances and Future Challenges. *Journal of Molecular Medicine* **2015**, *93*, 361–368, doi:10.1007/s00109-015-1269-z.
43. Taware, R.; Taunk, K.; Kumar, T.V.S.; Pereira, J.A.M.; Câmara, J.S.; Nagarajaram, H.A.; Kundu, G.C.; Rapole, S. Extracellular Volatilomic Alterations Induced by Hypoxia in Breast Cancer Cells. *Metabolomics* **2020**, *16*, doi:10.1007/s11306-020-1635-x.
44. Majmundar, A.J.; Wong, W.J.; Simon, M.C. Hypoxia-Inducible Factors and the Response to Hypoxic Stress. *Molecular Cell* 2010, *40*, 294–309.
45. Stegen, S.; Laperre, K.; Eelen, G.; Rinaldi, G.; Fraisl, P.; Torrekens, S.; van Looveren, R.; Loopmans, S.; Bultynck, G.; Vinckier, S.; et al. HIF-1α Metabolically Controls Collagen Synthesis and Modification in Chondrocytes. *Nature* **2019**, *565*, 511–515, doi:10.1038/s41586-019-0874-3.
46. Ito, K.; Kitajima, Y.; Kai, K.; Matsufuji, S.; Yamada, K.; Egawa, N.; Kitagawa, H.; Okuyama, K.; Tanaka, T.; Noshiro, H. Matrix Metalloproteinase-1 Expression Is Regulated by HIF-1-dependent and Epigenetic Mechanisms and Serves a Tumor-suppressive Role in Gastric Cancer Progression. *International Journal of Oncology* **2021**, *59*, 102, doi:10.3892/ijo.2021.5282.
47. Overall, C.M.; López-Otín, C. Strategies for MMP Inhibition in Cancer: Innovations for the Post-Trial Era. *Nature Reviews Cancer* **2002**, *2*, 657–672, doi:10.1038/nrc884.
48. Cui, H.; Grosso, S.; Schelter, F.; Mari, B.; Krüger, A. On the Pro-Metastatic Stress Response to Cancer Therapies: Evidence for a Positive Co-Operation between TIMP-1, HIF-1α, and MiR-210. *Frontiers in Pharmacology* **2012**, *3 JUL*, doi:10.3389/fphar.2012.00134.
49. Gholami, A.M.; Hahne, H.; Wu, Z.; Auer, F.J.; Meng, C.; Wilhelm, M.; Kuster, B. Global Proteome Analysis of the NCI-60 Cell Line Panel. *Cell Reports* **2013**, *4*, 609–620, doi:10.1016/j.celrep.2013.07.018.
50. Hurwitz, S.N.; Meckes, D.G. Extracellular Vesicle Integrins Distinguish Unique Cancers. *Proteomes* **2019**, *7*, 14, doi:10.3390/proteomes7020014.
51. Nolte, M.A.; Nolte-'t Hoen, E.N.M.; Margadant, C. Integrins Control Vesicular Trafficking; New Tricks for Old Dogs. *Trends in Biochemical Sciences* **2021**, *46*, 124–137, doi:10.1016/j.tibs.2020.09.001.
52. Soung, Y.H.; Ford, S.; Yan, C.; Chung, J. Roles of Integrins in Regulating Metastatic Potentials of Cancer Cell Derived Exosomes. *Molecular and Cellular Toxicology* 2019, *15*, 233–237.
53. Montenegro, C.F.; Casali, B.C.; Lino, R.L.B.; Pachane, B.C.; Santos, P.K.; Horwitz, A.R.; Selistre-De-Araujo, H.S.; Lamers, M.L. Inhibition of Avβ3 Integrin Induces Loss of Cell Directionality of Oral Squamous Carcinoma Cells (OSCC). *PLoS ONE* **2017**, *12*, doi:10.1371/journal.pone.0176226.
54. DeRita, R.M.; Sayeed, A.; Garcia, V.; Krishn, S.R.; Shields, C.D.; Sarker, S.; Friedman, A.; McCue, P.; Molugu, S.K.; Rodeck, U.; et al. Tumor-Derived Extracellular Vesicles Require B1 Integrins to Promote Anchorage-Independent Growth. *iScience* **2019**, *14*, 199–209, doi:10.1016/j.isci.2019.03.022.
55. Carter, R.Z.; Micocci, K.C.; Natoli, A.; Redvers, R.P.; Paquet-Fifield, S.; Martin, A.C.B.M.; Denoyer, D.; Ling, X.; Kim, S.H.; Tomasin, R.; et al. Tumour but Not Stromal Expression of β 3 Integrin Is Essential, and Is Required Early, for Spontaneous Dissemination of Bone-Metastatic Breast Cancer. *Journal of Pathology* **2015**, *235*, 760–772, doi:10.1002/path.4490.

56. Moritz, M.N.O.; Merkel, A.R.; Feldman, E.G.; Selistre-de-Araujo, H.S.; Rhoades (Sterling), J.A. Biphasic A2β1 Integrin Expression in Breast Cancer Metastasis to Bone. *International Journal of Molecular Sciences* **2021**, *22*, 6906, doi:10.3390/ijms22136906.
57. dos Santos, P.K.; Altei, W.F.; Danilucci, T.M.; Lino, R.L.B.; Pachane, B.C.; Nunes, A.C.C.; Selistre-de-Araujo, H.S. Alternagin-C (ALT-C), a Disintegrin-like Protein, Attenuates Alpha2beta1 Integrin and VEGF Receptor 2 Signaling Resulting in Angiogenesis Inhibition. *Biochimie* **2020**, *174*, 144–158, doi:10.1016/j.biochi.2020.04.023.
58. Danilucci, T.M.; Santos, P.K.; Pachane, B.C.; Pisani, G.F.D.; Lino, R.L.B.; Casali, B.C.; Altei, W.F.; Selistre-de-Araujo, H.S. Recombinant RGD-Disintegrin DisBa-01 Blocks Integrin Avβ3 and Impairs VEGF Signaling in Endothelial Cells. *Cell Communication and Signaling* **2019**, *17*, 27, doi:10.1186/s12964-019-0339-1.
59. Shattil, S.J.; Kim, C.; Ginsberg, M.H. The Final Steps of Integrin Activation: The End Game. *Nature Reviews Molecular Cell Biology* **2010**, *11*, 288–300, doi:10.1038/nrm2871.
60. Geiger, F.; Rüdiger, D.; Zahler, S.; Engelke, H. Fiber Stiffness, Pore Size and Adhesion Control Migratory Phenotype of MDA-MB-231 Cells in Collagen Gels. *PLoS ONE* **2019**, *14*, doi:10.1371/journal.pone.0225215.
61. Strande, V.; Canelle, L.; Tastet, C.; Burlet-Schiltz, O.; Monsarrat, B.; Hondermarck, H. The Proteome of the Human Breast Cancer Cell Line MDA-MB-231: Analysis by LTQ-Orbitrap Mass Spectrometry. *Proteomics - Clinical Applications* **2009**, *3*, 41–50, doi:10.1002/prca.200800083.
62. Bernhardt, S.; Tönsing, C.; Mitra, D.; Erdem, N.; Müller-Decker, K.; Korf, U.; Kreutz, C.; Timmer, J.; Wiemann, S. Functional Proteomics of Breast Cancer Metabolism Identifies GLUL as Responder during Hypoxic Adaptation. *Journal of Proteome Research* **2019**, *18*, 1352–1362, doi:10.1021/acs.jproteome.8b00944.
63. Sesé, M.; Fuentes, P.; Esteve-Codina, A.; Béjar, E.; McGrail, K.; Thomas, G.; Aasen, T.; Ramón y Cajal, S. Hypoxia-Mediated Translational Activation of ITGB3 in Breast Cancer Cells Enhances TGF-β Signaling and Malignant Features in Vitro and in Vivo. *Oncotarget* **2017**, *8*, 114856–114876, doi:10.18632/oncotarget.23145.
64. Grayson, W.L.; Zhao, F.; Bunnell, B.; Ma, T. Hypoxia Enhances Proliferation and Tissue Formation of Human Mesenchymal Stem Cells. *Biochemical and Biophysical Research Communications* **2007**, *358*, 948–953, doi:10.1016/j.bbrc.2007.05.054.
65. Schmaltz, C.; Hardenbergh, P.H.; Wells, A.; Fisher, D.E. Regulation of Proliferation-Survival Decisions during Tumor Cell Hypoxia. *Molecular and Cellular Biology* **1998**, *18*, 2845–2854, doi:10.1128/mcb.18.5.2845.
66. Hannafon, B.N.; Gin, A.L.; Xu, Y.; Bruns, M.; Calloway, C.L.; Ding, W. Metastasis-Associated Protein 1 (MTA1) Is Transferred by Exosomes and Contributes to the Regulation of Hypoxia and Estrogen Signaling in Breast Cancer Cells. *Cell Communication and Signaling* **2019**, *17*, 13, doi:10.1186/s12964-019-0325-7.
67. Casali, B.C.; Gozzer, L.T.; Baptista, M.P.; Altei, W.F.; Selistre-De-araújo, H.S. The Effects of Avβ3 Integrin Blockage in Breast Tumor and Endothelial Cells under Hypoxia In Vitro. *International Journal of Molecular Sciences* **2022**, *23*, doi:10.3390/ijms23031745.
68. Bos, R.; van der Groep, P.; Greijer, A.E.; Shvarts, A.; Meijer, S.; Pinedo, H.M.; Semenza, G.L.; van Diest, P.J.; van der Wall, E. Levels of Hypoxia-Inducible Factor-1α Independently Predict Prognosis in Patients with Lymph Node Negative Breast Carcinoma. *Cancer* **2003**, *97*, 1573–1581, doi:10.1002/cncr.11246.
69. Rana, N.K.; Singh, P.; Koch, B. CoCl2 Simulated Hypoxia Induce Cell Proliferation and Alter the Expression Pattern of Hypoxia Associated Genes Involved in Angiogenesis and Apoptosis. *Biological Research* **2019**, *52*, 12, doi:10.1186/s40659-019-0221-z.